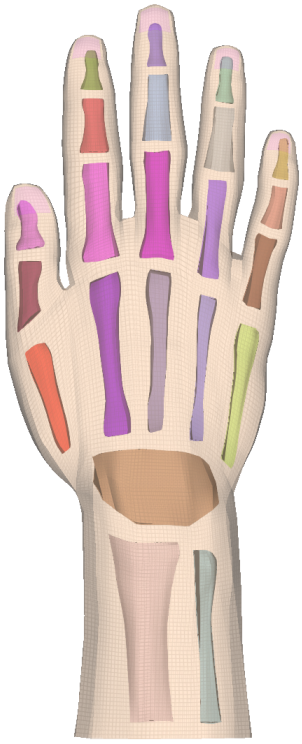

Development and Tuning of a Finite Element Average Human Hand Model

To support research and development of healthcare products for medtech applications

Master's thesis in Mobility Engineering

ELIN MASKOVA

DEPARTMENT OF MECHANICS AND MARITIME SCIENCES

CHALMERS UNIVERSITY OF TECHNOLOGY
Gothenburg, Sweden 2026
www.chalmers.se

Master's thesis 2026

Development and Tuning of a Finite Element Average Human Hand Model

To support research and development of healthcare products for medtech applications

ELIN MASKOVA

CHALMERS
UNIVERSITY OF TECHNOLOGY

Department of Mechanics and Maritime Sciences
Division of Vehicle Safety
Injury Prevention
Chalmers University of Technology
Gothenburg, Sweden 2026

Development and Tuning of a Finite Element Average Human Hand Model
To support research and development of healthcare products for medtech applications
ELIN MASKOVA

Supervisor: Dr. Alit Putra, Mölnlycke Health Care
Dr. Johan Iraeus, Department of Mechanics and Maritime Sciences
Examiner: Dr. Johan Davidsson, Department of Mechanics and Maritime Sciences

Master's Thesis 2026
Department of Mechanics and Maritime Sciences
Division of Vehicle Safety
Injury Prevention
Chalmers University of Technology
SE-412 96 Gothenburg
Telephone +46 31 772 1000

Cover: Dorsal view of developed FE average human hand model

Typeset in LaTeX
Printed by Chalmers Reproservice
Gothenburg, Sweden 2026

Development and Tuning of a Finite Element Average Human Hand Model
To support research and development of healthcare products for medtech applications
ELIN MASKOVA
Department of Mechanics and Maritime Sciences
Chalmers University of Technology

Abstract

The human hand is an essential part in our daily lives and a vital sense in how we feel and interact with the environment around us. However, ergonomic discomfort and pain remains prevalent in workplace and healthcare settings. To tackle these challenges, computer models of anatomical human hands can provide valuable insight into hand structure and object interaction that can support medical product development. This thesis documents the development of an anatomically based finite element (FE) average human hand model designed for applications within research and development for MedTech products.
The developed model incorporates derived skin geometry from magnetic resonance imaging (MRI) with open-source skeletal components to match a statistical average hand size. The meshing strategy focuses on a hexahedral model which can aid in future morphing of the geometry. A tetrahedral model was also constructed but only for a comparative study against the hexahedral model. Different constitutive models were investigated for the skin and soft-tissue behaviours, primarily consisting of viscoelastic and hyperelastic material models. Joints were modelled using a kinematic approach, using constraint-based rigid wire connections to enable biofidelic positioning.
Parameter tuning was performed with published experimental data that tested the finger pulp compression at selected loading rates of 0.1 and 0.3 mm/s. Simulation results depicted similar mechanical behaviour as experimental tests but an additional dataset would be required to fully validate the model. The study outlines the steps taken along with the models used to construct a feasible anatomical human hand FE model for product interactions. Although the current model has its limitations, a single size and simplified anatomical structure (no muscles, ligaments or tendons modelled), it lays a good foundation for future morphing capabilities and a broad analysis for healthcare product investigation and development.

Keywords: finite element, human hand model, hexahedral, ergonomic, discomfort, healthcare

Acknowledgements

I would like to express my utmost gratitude to my industrial supervisor, Dr. Alit Putra, at Mölnlycke Health Care for guiding, teaching and assisting me throughout this Master's thesis project. I would also like to thank all other colleagues at Mölnlycke, more notably Johannes Vigmo, MSc and my team manager Océane Khilstrand, MSc. You all warmly welcomed me into your new office and allowed me to develop myself, learning new software and topics such as FEM. You also gave me the opportunity to gain a better insight into the MedTech world, with real world applications of the topics I was learning.
Another big shout out is necessary for my Chalmers support group consisting of: my supervisor Dr. Johan Iraeus, examiner Dr. Johan Davidsson, and hexablock master and mentor Dr. Jobin John. You all provided your expertise and allowed me to grow as a researcher and student.
Additionally, I would like to thank, BETA CAE Nordic AB for providing me with free academic ANSA and META software on behalf of Dr. Stylianos Seitanis.
Your support played a vital role in my success and completion of this project. I want to thank you all for letting me learn, make mistakes and develop myself further.

Elin Maskova, Gothenburg, January 2026

List of Acronyms

Below is the list of acronyms that have been used throughout this thesis listed in alphabetical order:

CORA	CORrelation and Analysis
CT	Computer Topography
DIP	Distal InterPhalangeal joint
DoF	Degrees of Freedom
FE	Finite Element
FEM	Finite Element Method
HBM	Human Body Model
MCP	MetaCarpoPhalangeal joint
MRI	Magnetic Resonance Imaging
PIP	Proximal InterPhalangeal joint
PIPER	Position and Personalize Advanced Human Body Models for Injury Prediction
THUMS	Total HUman Model for Safety
VIVA+	Open source human body model for injury prevention
2D	Two dimensional
3D	Three dimensional

Nomenclature

Below is the nomenclature of indices, sets, parameters, and variables that have been used throughout this thesis.

Variables

t	Time
l_c	Size of element
ρ	Density of material
E	Young's modulus (stiffness of material)
ϵ	Dimensionless strain
σ	Stress
ν	Poisson's ratio

Contents

List of Figures

List of Tables

1
Introduction

1.1 Background

Touch plays a vital role in how we interact with the environment around us. Through touch, more specifically with our hands, we manipulate tools and realize daily actions like eating. An important aspect in hand-object interactions, especially in the workplace, is hand fatigue and wearable devices.

1.1.1 Ergonomic Hand Comfort Problems

In the medical product field, one example of ergonomic hand problems is the utilization of examination gloves, where around 32% of medical professional respondents noted issues with the fit. This issue with glove fit can introduce significant ergonomic and comfort issues that can lead to the loss of tactility or even tearing [7]. This not only compromises workflow but presents one of many examples where ergonomic and comfort issues arises within the medical product field. Generally, this hand discomfort can be associated with mechanical stresses and the deformation of various biological tissues [8]. Therefore, a company can address ergonomics by analyzing a products interaction with the user by creating computer models and simulations, which can allow the cost of developing products to be decreased as well as lowering designing time [9]. Within the MedTech sector, many companies are investing in digital tools and using simulation driven development. As part of this general industry trend, the creation of anatomically based Finite Element (FE) models has become increasingly relevant for improving product design and ergonomics. Therefore, the work outlined in this thesis will focus on the process of creating a FE hand model.

1.1.2 Existing solutions

Many existing approaches that aim to address hand comfort problems are done by using computer models, known specifically as biomechanical models, which can be highly complex. This complexity introduces variation in approaches with the four main types of models being: lumped parameter models, multi-body models, Finite Element models, and hybrid models which can be any combination of the aforementioned types [8]. The composition (level of detail and biological components) of a model relates to the desired analysis, however, both a correct anatomical shape and kinematics is important in achieving accurate bio-mechanical responses in computer models [9].

1.2 Objectives

Existing FE hand models vary extensively in geometric biofidelity, material models, and validation testing. Most focus on grasping objects, without morphing capabilities or without investigating low-rate fingertip compressive validation experiments. Overall, a wealth of knowledge and models within this research area exists, but, the lack of available full human hand models for comfort analysis leads us to address the following objectives:

1.2.1 Primary Objective:

Develop and tune an anatomically based Finite Element human hand model to support product research and development within the medtech sector.

1.2.2 Secondary Objectives:

- **Integrate** realistic geometry and derive development steps to match target average human hand dimensions.
- **Implement and compare** physically motivated material models and select a baseline.
- **Develop a method to reposition** the baseline hand posture to another posture (e.g. precision pinch) with biofidelic movement.
- **Support** future morphing capabilities for different hand sizes.

1.3 Scope

The developed model is limited to one specific hand size and therefore does not investigate variations, such as age, sex or size (referred to as morphing). The distinction between muscles and fat, as well as the inclusion of other details such as nerves or blood vessels was not considered due to the complexity and lack of necessity for this specific application. During the modelling stage, some additional geometric simplifications were introduced in regions outside the area of interest (e.g., forearm and wrist). No model validation (experiments or simulations) was performed, only previously calibrated material models from literature were used to tune the model.

2

Theory

Hands are very complex with haptic perception and motion control being essential but not limited to applications such as bionic and robotic arms, where computer models are used to simulate scenarios [10]. Other applications such as clothing, wearable devices and surgical planning have also started to incorporate computer models over the past two decades [11], [12], [13]. This chapter will outline the fundamentals of human hand anatomy, finite element models and existing human body model (HBM) frameworks that are essential for understanding the contents of this thesis.

2.1 Human Hand Anatomy and Mechanics

The study of human hand anatomy dates back to prehistoric times, but our knowledge and models still require improvement due to the intricate combination of bones, muscles, veins, tendons, ligaments, joints and skin that are present. The human hand skeleton, as shown in Figure 2.1, is comprised of 27 bones with countless degrees of freedom (DoF). Generally, the bones can be split into three groups; the `carpals` which are the 8 wrist bones, the `metacarpals` which are the 5 intermediate bones between the wrist and fingers, and the `phalanges` which are the 14 finger bones [14]. The radius and ulna are bones in the forearm.

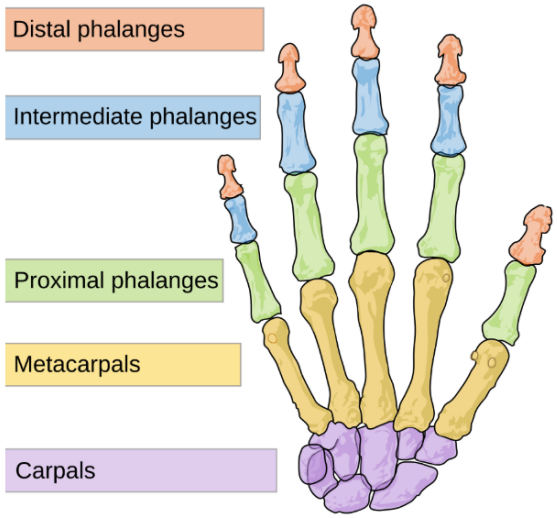

Figure 2.1: Labelled human hand skeleton. [2], PD

The muscles in the hand can be grouped into extrinsic and intrinsic muscles [14]. Most extrinsic muscles originate in the forearm however intrinsic muscles are solely

confined to the wrist and hand [15]. The movement and combination of these muscles plays an important role in how the hand moves.
The tendons in the hand and body connect muscle to bone, allowing to move the skeleton by transmitting the muscles forces to the respective bones. Ligaments on the other hand connect bone to bone, keeping structures stable and in place [3]. A visual comparison of the two can be seen in Figure 2.2.

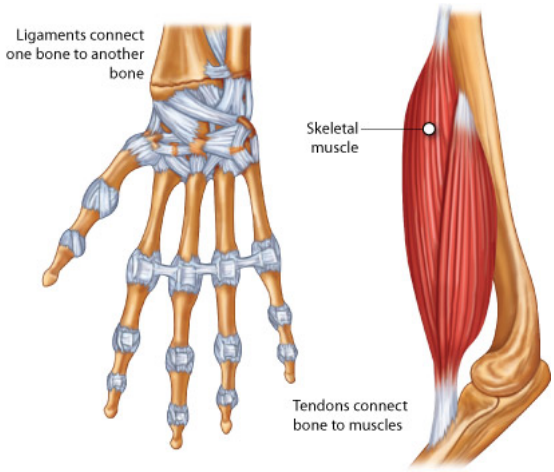

Figure 2.2: Tendon versus ligament schematic. [3], CC BY-NC-SA 4.0

Other components in the hand are nerves which are important for transmitting sensory information and veins which carry blood around the body [14]. In addition, there is a layer of subcutaneous fat/tissues under the layer of skin which varies in thickness across the hand (relatively thick on the palmar side in comparison to the thinner and more pliable soft dorsal side) [15].

2.2 Finite Element Fundamentals

The Finite Element Method (FEM) is a general method to approximately solve differential equations where analytical solutions do not exist. They can be used to describe for example a complex mechanical system such as the human body. Elements are the resulting area between nodes which are discrete points placed along and in the geometry to best capture the actual shape. Each element holds information about how its nodes are connected to others. This means that the structure is coupled and that each interaction will result in the movement of multiple nodes. The shape of the parts being modeled commonly uses three types of elements: beam (line, long and slender structures), shells (2D elements) and solids (3D elements). The constitutive behavior of elements (stress vs. strain) is defined by material models which make up a core component in FE codes [16].
Within FEM, there exists two main types of solvers: **explicit** and **implicit**.

- **Explicit**:
  Typically used to solve highly non-linear material models and complex contacts with small time-steps like car crash simulations [16]. The smaller the element

size, the smaller the timestep, as governed by the stable timestep criteria given by,

$$\Delta t \leq l_c \sqrt{\frac{\rho(1-\nu^2)}{E}}. \tag{2.1}$$

- **Implicit**:
  Allows for larger time-steps due to no limitations from a timestep stability. It is more computationally expensive for each incremental calculation so implicit solvers are generally used for static or quasi-static simulations [17].

2.2.1 Material constitutive behaviour

Using mathematical models to describe the mechanical properties/behaviours of materials tested experimentally is known as constitutive modelling. This is generally described with stress-strain relationships. Human tissues can be characterized (in general) with six different types of materials [18]. These are as follows:

1. **Linear elastic:**
   material will return to its original shape after the external load is removed. The linear relationship is described by the constant, Young's modulus (E).
2. **Elastic-plastic:**
   combination of elastic (returns to original shape after loading is removed) and plastic (undergoes irreversible deformation due to loading) properties where a yield point separates the two regions.
3. **Hyperelastic:**
   it can sustain a very large deformation and still recover fully once loading has stopped. This material type has many different modelling types for the strain energy potential, including examples such as Mooney-Rivlin, Ogden and many more.
4. **Viscoelastic:**
   combination of viscous (deforms slowly under an external force) and elastic (returns to original shape after loading is removed) properties. They form a hysteresis stress-strain loop with the area in the loop representing energy dissipated as heat.
5. **Orthotropic:**
   properties differ along three orthogonal axes.
6. **Foam:**
   when subjected to compressive loading it usually exhibits three characteristic responses, including linearity, plasticity-like stress plateau and densification stages.

2.3 Existing Human Hand Models

Various models with distinct focuses exist to date. Cei et al. [19], looked at 76 specifically selected haptic interaction finger/hand model studies and compared them on the basis of geometric, biomechanical and interaction complexities. Their review

shows the large variation of models that exist and they noted that work on joints, friction and anisotropy of skin are still lacking in current literature.

Physics based models such as a mass-spring system with a hybrid muscle model has been used by Albrecht et al. [13] to model an anatomical human hand. They state that the physics based approach results in animations that are anatomically and physically correct by default. Their hybrid muscle model is a combination of pseudo muscles which are used to control the rotation of the bones by converting a contraction value (range $C \in [0, 1]$ where 0 is no muscle contraction and 1 is a full muscle contraction) to a joint rotation angle and geometric muscles which account for skin deformations as they bulge and deform.

More recent studies tend to focus on creating FE hand models for simulating grasping situations in the aim of improving object ergonomics for improved hand comfort and function. Harih & Tada [20], tested and validated not only common grasping shapes such as a cylinder (commonly used in handles for all kinds of tools), where cylindrical, spherical and precision shapes are the three most common in our daily lives [10] but also a Stanford Bunny which represents an organic non-standard shape. Their FE digital human hand model showed to be numerically feasible and stable and could be used to simulate grasping common and organic shapes with reasonable biomechanical responses. In another article, Harih et al. [21], investigate ergonomic 3D FE hand-product simulations, where they focus on mechanical loads of soft tissues, mainly comprising of contact areas and pressures. Although a promising model, they model the skin and soft tissue as Ogden hyper-elastic materials, neglecting the effects of viscosity. Viscous effects are however an equally important aspect in the non-linear visco-elastic behaviour of the skin and subcutaneous tissue, especially for accurate tissue pressure and comfort analysis.

Other interactions besides grasping which most frequently use FE simulations include encompassing/surface objects such as pressure therapy garments or general clothing pressure prediction. These garment models do not only have contacts with the hand model but can also deform the hand/body [11]. This deformation introduces some challenges into the FE model of both the hand/body and the object, because the model needs to ensure the desired output is set within the boundary conditions [12]. Additionally, since these models focus on external contact and deformation between the hand and garment, they generally use simplified hand models, like Yu et al [12], that model the hand as one part (no separation of parts like bones, skin, etc.) and assume all components to be homogeneous, isotropic and linearly elastic.

Various human body models exist for hands and full bodies [22], with some full body open source FE models available from crash-test developments, such as **VIVA+** [23], **PIPER** [24] and **THUMS** (from Toyota) [25] to name a few. Commercial options also exist including the **Virtual Population (ViP)** [26] developed in Switzerland. For this thesis, an internal industry model comprising of a simplified and anatomical human hand model will be combined with other open source human body models.

2.3.1 Geometry

For any mechanical model, a geometrical representation is needed. Generally, studies use different imaging methods on living subjects depending on funding, available

machinery/measurement tools and the desired model focus. Some common imaging methods include: Computer Topography (CT) (when accurate bone geometry is desired) [27], [21], Magnetic Resonance Imaging (MRI) with segmenting (when accuracy and separation of soft tissues is required) [28], and photography with measurements (for external hand measurements) [29]. One study used imaging methods on a cadaver instead of living subjects to create a 3D digitization into a linked segment model where they focused on the muscles (extrinsic vs intrinsic) [30].

2.3.2 Joint Modelling

Different approaches also exist for finger joint modelling, of which all investigated literature used kinematic joints. The majority used a similar approach of creating a new local coordinate system, with two reference points connected by a rigid wire and using constraints to model the joints [9],[20],[21],[11],[10]. Two articles used hinge and universal joints, [5],[8], and one used a more complex joint modelling technique, where they modelled the bones, cartilage, capsules, skin and used contact pairs to limit penetration of nodes with tie connections to keep components connected/moving together [31]. Furthermore, one study used an instrumented glove (Cyberglove II), to gather data on finger joints and hand movements [32].

2.4 Statistical analysis

To compare the model output to the experimental data, the CORA (Correlation and Analysis) method is used. Note, differences between experimental and simulation time lengths needed to be adjusted before the CORA python functions could be used.
The CORA method assesses the similarity between two time-history signals (typically the reference one is from experiments and the comparative one from simulations), with a resulting value, known as the CORA score, ranging from 0 to 1, where 1 is a perfect match within the specified tolerances and 0 is a poor match. The interval of evaluation, $[t_{min}, t_{max}]$, is the time range in which the calculation is conducted. The signal similarity is evaluated through two complementary metrics: the corridor method and the cross-correlation method [33].
First, the corridor method uses a corridor fitting to calculate the deviation between both signals. It places four curves, inner and outer tolerance corridors around the reference signal. If the other curve fits within the inner corridor the result is 1, if it falls outside the outer tolerances it results in a value of 0, otherwise an interpolation is done for each time step in the interval of evaluation. The overall corridor rating is a mean of all individual time-step values [33].
Second, the cross-correlation metric takes into account those areas not considered in the corridor method, differences in phase, magnitude and shape. The reference curve is shifted in increments of the time step (Δt) each time calculating the cross correlation within the entire specified time range (interval of evaluation). The values for phase, magnitude and shape are calculated for the time-shift that results in the maximum cross-correlation. The total cross correlation value is a result of calculating the weighted sum of all three values [33].

The overall CORA score is then a weighted sum (user-defined) of the corridor and cross-correlation values [33]. The CORA score is also given a classification as defined below:

- CORA score $\geq 0.9 \Rightarrow$ Excellent
- CORA score $\geq 0.7 \Rightarrow$ Good
- CORA score $\geq 0.5 \Rightarrow$ Acceptable
- CORA score $< 0.5 \Rightarrow$ Poor

3

Methods

This chapter will outline the steps and approaches taken throughout this Master's thesis project. The main emphasis being the modelling of an anatomical Finite-Element human hand model where Figure 3.1 shows an overview of the modelling process. The software used for this project includes: ANSA version 24.1.5 (BETA CAE Systems, Thessaloniki, Greece) for pre-processing tasks such as geometry preparation and meshing, ABAQUS 2022 (Dassault Systèmes, Vélizy-Villacoublay, France) for simulation preparation tasks such as material model implementations and model positioning, and META version 23.1.4 (BETA CAE Systems, Thessaloniki, Greece) for post-processing tasks along with Excel and Python (Spyder IDE) for data cleaning and plotting.

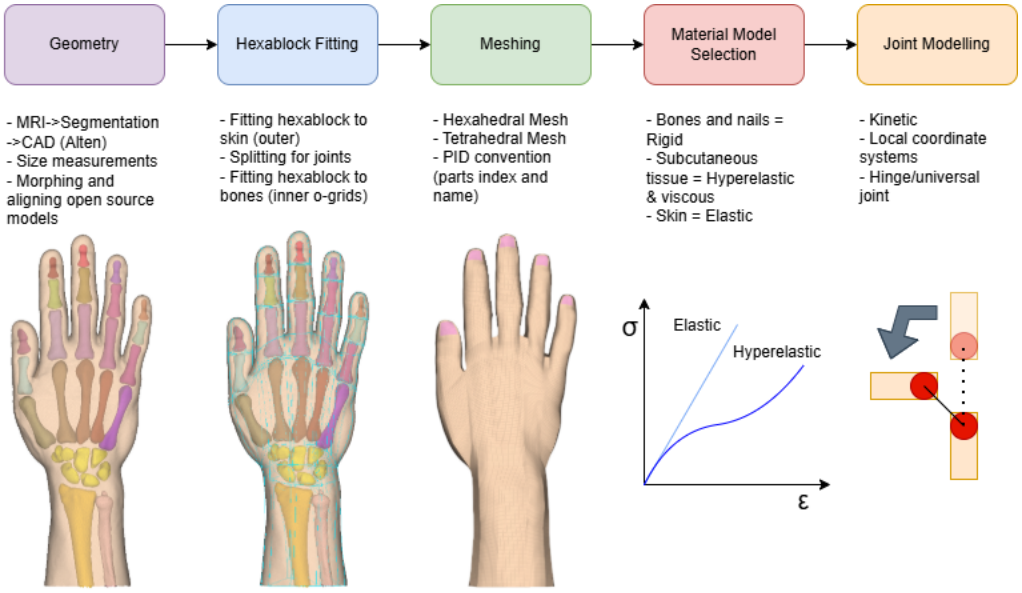

Figure 3.1: Modelling flowchart

3.1 Geometry: model sources and integration

An extensive internal industry dataset containing 3D scans and anthropometric measurements was used to define the target hand size. Table 3.1 summarizes the base hand model dimensions, where the measuring and naming scheme is shown in Figure 3.2. Futhermore, the MRI scan used for creating the CAD geometry was

obtained from an individual whose hand dimensions closely matched the selected target size.

Table 3.1: Base measurements used for hand model

Measurement Name	Identifier	Value (mm)
Finger Lengths	F1-L	60
	F2-L	70
	F3-L	78
	F4-L	71
	F5-L	57
Palm Width	P-W1	84
Palm Length	P-L1	105
Wrist Circumference	F-C1	169

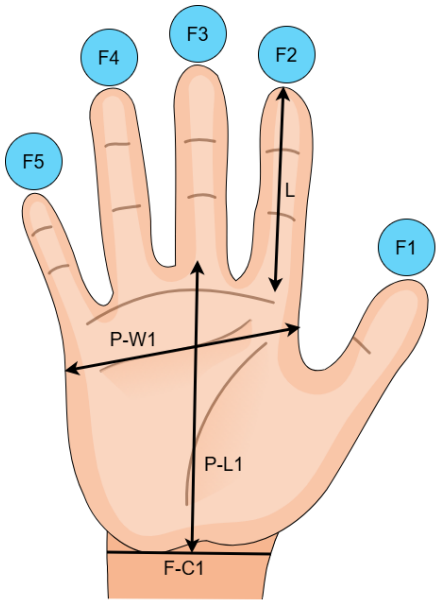

Figure 3.2: Hand measurement and naming convention. [4], CC0, changes made.

However, some discrepancies in geometric biofidelity of the original MRI model were identified. Adjustments to bone shape were necessary, with some open source models being investigated. The two main models are the Open Hands (version 2024-07) model [27] (CC BY-SA 4.0 license) and the 56 year old female reference PIPER model [24] (CC BY 4.0 license). Model measurements (lengths and circumferences) of the outer skin and internal bones were conducted on the original geometry model and open source models. Of these, the original geometry was taken as the true target size, so the difference to the other models was calculated. From these calculations, a selection of which parts were to be replaced was made and it was decided to keep the original MRI skin geometry and only replace the bones.
The chosen model parts and respective changes are summarized in Table 3.2. The main methodology behind the changes is that the Open Hands model has a biofidelic

shape of the phalanges with desired bone size, but only models fingers 2-5. These bones were therefore directly imported into the original geometry and aligned at the place of the existing bones. For the thumb and metacarpals, the PIPER reference model (referred to as PIPER ref) was chosen. This choice occurred as the bone shape was more accurate than the original geometry, but the bones were smaller in size, so a morphing of extending the bone length was necessary. The morphed bones were then aligned into the correct position and some additional adjustments to reduce bone gaps and intersecting parts were conducted. The radius and ulna were directly imported from the PIPER reference model and the carpals were kept from the original model but grouped as one part instead of 8 separate bones.

Table 3.2: Model choice and respective changes for different bones

Part	**Chosen Model**	**Changes**
Phalanges (F2-F5)	Open Hands	Aligned
Thumb (F1)	PIPER ref	Morphed (length stretched) and aligned
Metacarpals	PIPER ref	Morphed (length stretched) and aligned
Radius	PIPER ref	Aligned
Ulna	PIPER ref	Aligned
Carpals (8 wrist bones)	Original	Grouped into one part

3.2 Meshing Strategy

Once the geometry is established, the next step is to create a mesh. For this, there are two commonly used types; the hexahedral and tetrahedral mesh. The base 3D building block shape of each is shown in Figure 3.3a and Figure 3.3c respectively. Besides the obvious difference in shape, each mesh has its own advantages and disadvantages as highlighted in Table 3.3. There, the main takeaways are that the hexahedral mesh has good morphing capabilities but is time consuming to manually fit the hexablock to the geometry. On the other hand, tetrahedral meshes are excellent at fitting irregular shapes (geometric accuracy) with fast automatic mesh generation.

Table 3.3: Comparison of mesh types

Mesh type	Advantages	Disadvantages
Hexahedral	Good for morphing Good numerical accuracy	Difficult to fit to complex geometries Loose geometric accuracy
Tetrahedral	Fits well to irregular shapes Fast automatic generation	More elements for same resolution Poor numerical convergence

To better illustrate the difference, Figure 3.3b and Figure 3.3d show the VIVA+ 50% percentile standing female hand model and 56 year old PIPER reference hand model as examples of the hexahedral and tetrahedral meshes respectively. It can be

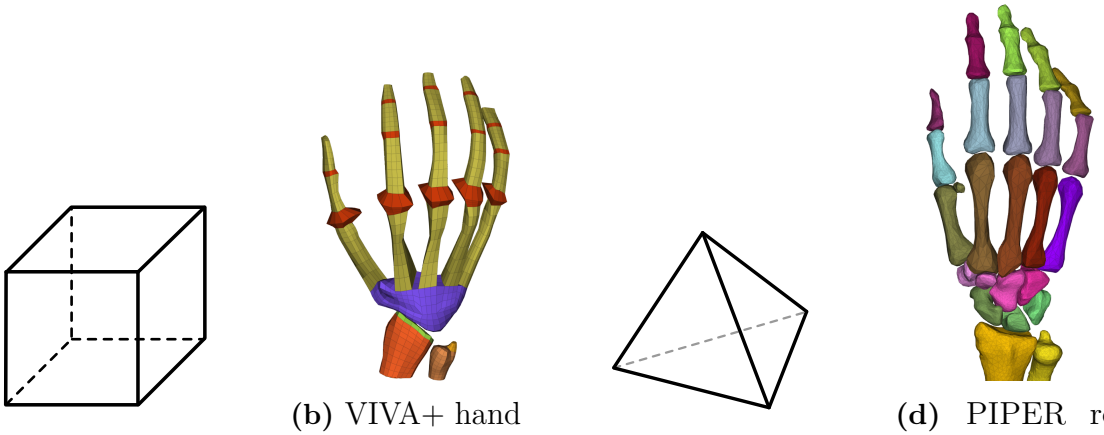

(a) Hexahedral shape. [34], CC0

(b) VIVA+ hand skeleton. [23], LGPL v3

(c) Tetrahedral shape. [35], CC0

(d) PIPER ref hand skeleton. [24], CC BY 4.0

Figure 3.3: Comparison of hexahedral and tetrahedral mesh shape with VIVA+ 50% percentile standing female hand model & 56 year old PIPER reference hand model as examples respectively.

noted that the VIVA+ bones look like rectangles (loose real bone shape), whereas the PIPER model has very accurate bone shapes, further showing the difference between model types. In terms of choosing the best model type for our model, we first chose to run simulations using Abaqus explicit, which generally limits the model to first order elements. Linear tetrahedral models converge slowly for stress and strain, which for our model is a desired analysis point, and therefore a drawback. Additionally, morphing and being able to change the size of the hand is the main desirability for future developments of the model. Therefore, this leads to the choice for a hexahedral mesh and although this is the main focus of this study, a tetrahedral mesh was also generated for a small comparative study.

For generating a hexahedral mesh, a hexablock needs to be manually fit to the geometry. The approach taken in this thesis was to work from the outside in, so to start by fitting the skin and then working inwards to the bones. Figure 3.4 shows the fully fitted hexablock as well as the internal (o-grid) fitting of the bones and joints. Fitting the hexablock to a complex geometry is a difficult task and it was the most time-consuming task in the modelling stage. Something to take into account when fitting a hexablock is to check the box quality, this ensures that the mesh will have a good quality and structure. We used the standard 20-160 degree box quality check with no errors but some off angle warnings. This is a trade-off between preserving the most accurate geometry and box/mesh quality, where compromises from both aspects were necessary.

Once the hexablock is fit, the hexahedral mesh can be generated and the size of the elements can be adjusted by changing the number of them. For this model, the desired element size was between 1-2 mm. After adjusting the hexahedral mesh to the target element size, a tetrahedral mesh was also generated. Components in each model were separated into their own PID as described by the naming convention in Table 3.4 (full table shown in Table A.1). The subcutaneous tissue in biological terms is the deepest part of the skin mainly comprising of fat tissues, however, in this case

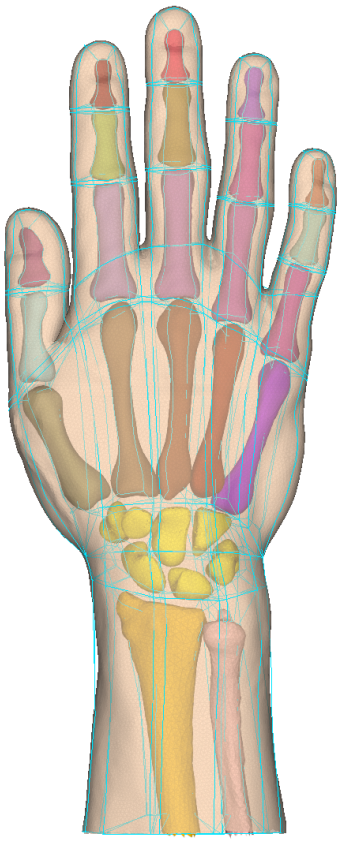

(a) Fitted full hand hexablock

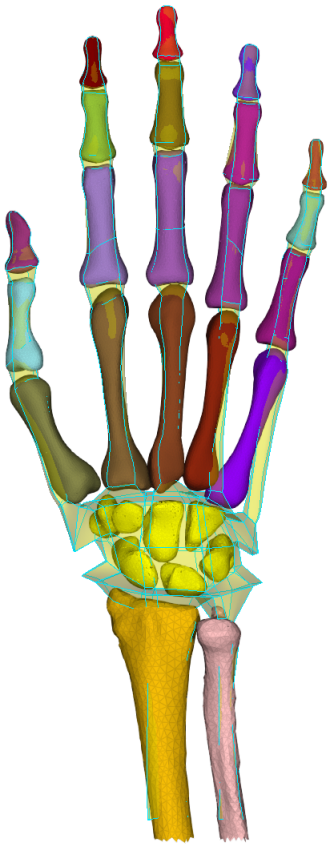

(b) Fitted internal bones hexablock

Figure 3.4: Fitted hexablocks

we consider the subcutaneous tissue as both the fat and muscle layers (everything between the bone and outer skin layer). An additional note is that the standard finger numbering considered throughout this thesis is as shown in Figure 3.2.

Table 3.4: Component identifiers and descriptions

Component Identifier	Description
1000	Skin
1001	Subcutaneous Tissue
1002	Radius
1003	Ulna
1004	Carpals
1005 - 1009	Metacarpals
1010 - 1023	Phalanges
1024	Nails

3.3 Constitutive Modelling

For all FE models, different components and their material behaviours need to be captured in so called material models. In our FE human hand model we will consider 4 components: skin, subcutaneous tissue, bone and nail. The skin and subcutaneous tissue exhibit complex behaviour, being heterogeneous and anisotropic, with nonlinear viscoelastic properties [36], [10]. On the other hand, the bones and nails can be considered homogeneous and rigid (not deform under loads)[11]. For modelling, two articles, from Wu & Harih separately, were chosen for their validated hand material models. Both articles use the same geometric setup but with different material models, each validated with experimental data. The derivations of each material model along with their parameter values is included in detail in the appendix (subsection A.2.1, subsection A.2.2). We will further mention the articles by referring to them as article 1 [1] by Wu et al and article 2 [36] by Harih and Dolšak. An overview of the different material models used for each model part is summarized in Table 3.5, where the models are separated by article (refer to number) or were the same for both articles.

3.4 Joint Kinematics Modelling

The desire for simulating various hand positions, such as a pinch grip, requires the model to be able to deform in a biofidelic way, leading to the need of implementation joints. Literature shows that kinematic finger joints are the most commonly used for hand modelling with biofidelic results. We will take the main approach as outlined by Wei et al. [5], by first deleting our temporary meshed joints and placing new local coordinate systems at 15 locations (all Proximal InterPhalangeal (PIP), Distal InterPhalangeal (DIP) and MetaCarpoPhalangeal (MCP) joints) as shown in Figure 3.5a. Next, two reference points are placed (one on each bone associated with the joint) and then a rigid wire is used to connect the two reference points together. Following this, a hinge joint (rotation about only 1 axis) gets assigned to each DIP and PIP joint and a universal joint (rotation about 2 axes) gets assigned to each MCP joint. Additionally, a spring stiffness is added to each joint to mimic the joint stiffness with the full joint implementation being shown in Figure 3.5b.

3.5 Model Tuning

Model tuning aims to fit the model to experimental data. This check ensures that the system is correctly modelled with realistic results, in our case called biofidelity. After an extensive literature search and review, it was determined that there are no articles that provide experimental data and tests on the full human hand, so the focus was shifted to only compressive fingertip tests at very slow loading rates (like 0.1 mm/s). The option for in-house volunteer experiments was investigated, but due to some ethical issues and time restraints this option was disregarded. In addition to selecting a specific target area and type of test, the target article would combine experimental tests and finger/hand models (including used and validated material

Table 3.5: Material model review

Part	Material Model	Model Thickness	Validation Tests
Subcutaneous tissue	**1.** *Viscoelastic* (constitutive equations) and *elastic* (polynomial model) with values from Table A.2, Table A.3 respectively. For elastic properties, different stiffness ratios (r) were tested to match experimental data from (Serina et al. 1997 [37]; Wu et al. 2003 [6]): $r = 1/8$ and $r = 1/4$ respectively	–	Finger compression tests (Serina et al. 1997 [37]; Wu et al. 2003 [6])
	2. *Ogden hyper-elastic model* with values from Table A.5 (Ali et al. 2010 [38]), and Poisson ratio of 0.4 (Wu et al. 2002 [39])	Roughly 1 mm	Uniaxial tensile test (Ali et al. 2010 [38]; Pan et al. 1998 [40])
Skin	**1.** Outer skin is *linear elastic*: Young's modulus of 2 MPa, Poisson ratio of 0.3 (Agache 2004 [41]). Inner skin with values from Table A.2, Table A.3	Outer skin: 100 µm; Inner skin: 1.2 mm	Inner skin: in vivo test data (Hendriks et al. 2003 [42], 2004 [43])
	2. *Ogden hyper-elastic model* with values from Table A.4 (Ali et al. 2010 [38]), and Poisson ratio of 0.4 (Wu et al. 2002 [39])	Roughly 4 mm at thickest point	Uniaxial tensile test (Ali et al. 2010 [38]; Pan et al. 1998 [40])
Bone	*Linear elastic*: Young's modulus of 17 GPa, Poisson ratio of 0.3	–	Yamada 1970 [44]
Nail	*Linear elastic*: Young's modulus of 170 MPa, Poisson ratio of 0.3	0.60 mm (Baran 2004 [45])	Yamada 1970 [44]

models). Over several articles, one author, Wu, performs compressive tests on an index finger with low loading rates [6] and uses this data to validate a 2D and 3D FE model of the index finger distal phalanx [46],[1].

3.5.1 Experimental Fingertip Compression Data

The chosen experimental data from [6], collected data from 4 subjects (2 male and 2 female) with an average age of 24 years old. They used the experimental setup

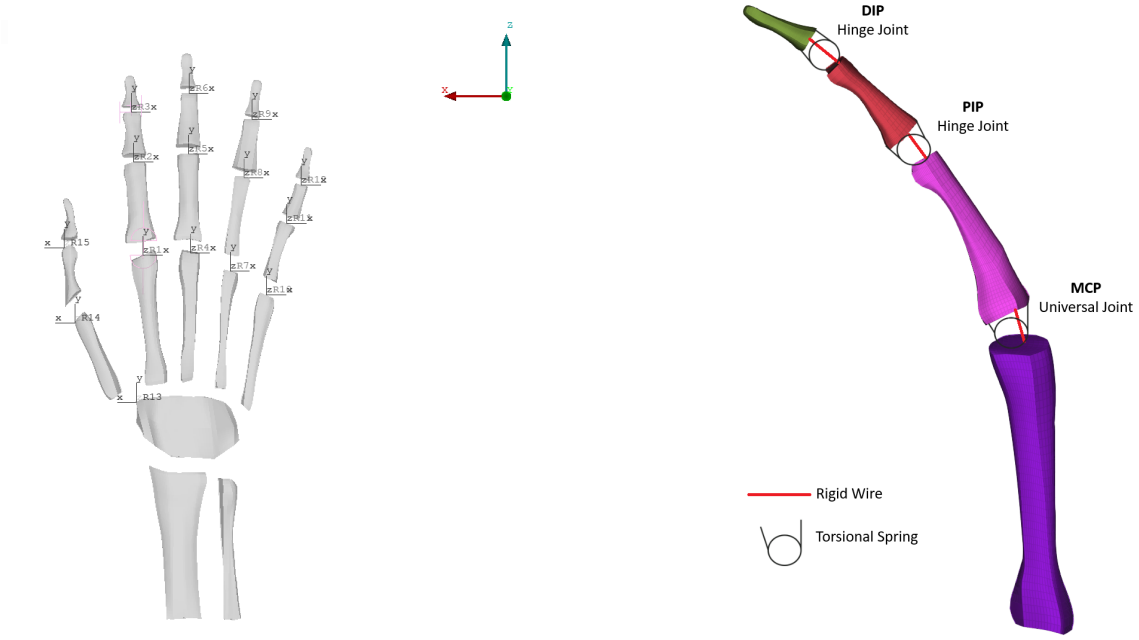

(a) Local coordinate system placement **(b)** Labelled joint model

Figure 3.5: Joint modelling with a) showing placement of local coordinate system and b) showing a depiction of the joint construction as inspired by [5]

shown in Figure 3.6, where they tested both the left and right index finger of the subjects. The experimental setup comprises of a 25 mm x 25 mm flat steel plate and finger hold that keeps the finger at roughly an angle of 20^o. The movement of the flat steel plate was generated by a universal micromechanical testing machine (Mach-I, Biosyntech, Montreal, Canada) which used a displacement-controlled protocol. To minimize effects of temperature differences between the steel plate and fingerpad, the flat plate was covered by a smooth plexiglass sheet (3 mm thick). Additionally, to ensure constant contact between the finger and the support throughout the entire test, a double-sided adhesive tape was applied on the nail and used to adhere the finger to the support. The author notes that the thickness of the tape (0.10 mm) is so small as compared to the finger, so any error caused by the deformation of the tape is not considered.
The experiments conducted consist of 2 series which are summarized as follows:

1. Series A:
    - Compression to 2 mm displacement with loading speeds of 0.1, 0.2, 0.4, 0.9, 1.5 and 5.7 mm/s
    - Hold at 2 mm displacement for 30 sec
    - Reduce to 1 mm displacement with 1 mm/s speed
    - Hold at 1 mm displacement for 30 sec
2. Series B:
    - Compression to 3 mm displacement with loading speeds of 0.3, 0.5, 0.9, 2.3 and 4 mm/s
    - Hold at 3 mm displacement for 30 sec
    - Reduce to 2 mm displacement with 1 mm/s speed

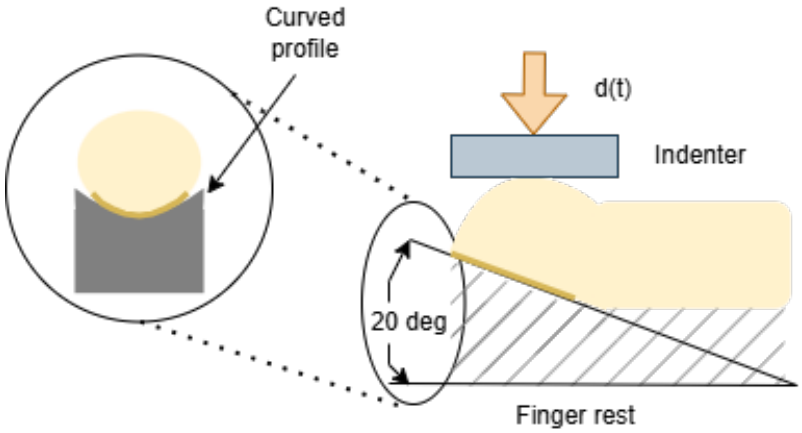

Figure 3.6: Fingertip experimental test setup from [6]

- Hold at 2 mm displacement for 30 sec

Since the focus was chosen to investigate the long-term exposure and compression of hands, the decision for slow loading rates and sustained compressive forces was ideal. Therefore, from all loading rates conducted in the article, we will solely focus on the speeds of 0.1 mm/s from Series A and 0.3 mm/s from Series B. The loading rates as described earlier are visualized in Figure 3.7a, where the distinction between series is shown. The force response of the 0.3 mm/s Series B loading curve with experimental bounds is shown in Figure 3.7b. There, as in the displacement loading curve, the four testing stages can be distinguished. Mapping these four testing stages to material properties, we see that the first rise in the non-linear force shows characteristics of both viscous and elastic effects. In the second stage, the viscous forces cause the force to decrease (known as creep) during the sustained compression. Then in the third stage, we see a fast linear shift to the second displacement, and finally, in the last step, we see some elastic recovery into a steady state as the second displacement is held. The oscillations in the measurements can be associated with involuntary muscle movement or blood flow as mentioned by the authors.

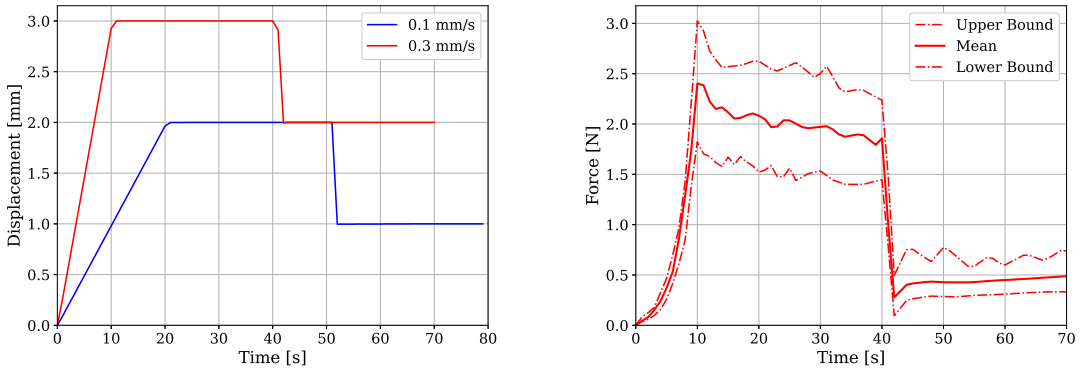

(a) Displacement loading curves **(b)** Force response for 0.3 mm/s

Figure 3.7: Experimental input for both series (a) and full force output with experimental bounds for 0.3 mm/s loading rate (b)

For our fingertip simulations, we would like to look at different relationships rather than the raw input and output data. Instead, we use the force vs. displacement curves as shown in Figure 3.8.

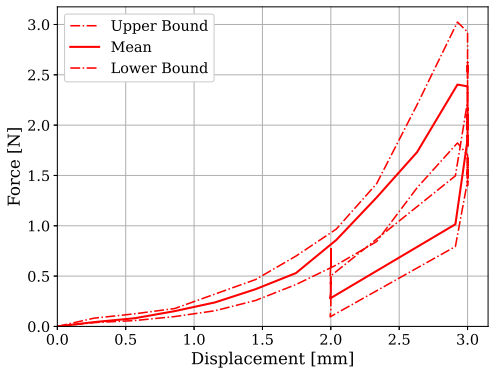

(a) Force vs. displacement with bounds for 0.3 mm/s

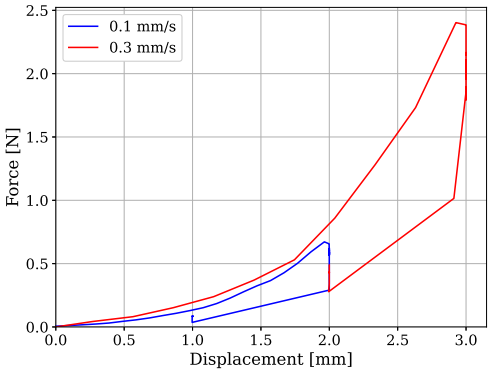

(b) Force vs. displacement for both series

Figure 3.8: Experimental force vs. displacement curves

3.5.2 Fingertip Simulations

The fingertip simulations for parameter tuning were setup in the same way as the experimental setup (Figure 3.6), with a flat plate that moves downward to compress the finger pulp and a 20 degrees angled finger holder. Since the indenter moves downward, the corresponding node that measures the force and displacement initially gives negative values. Before proceeding, these need to be filtered (CFC filter with value 1 Hz used), inverted and resampled.
The tests conducted are outlined in Table 3.6, where tests were first conducted with the Series B loading rate and then Series A. A note however is that not all six tests (generally with multiple rounds) were conducted on both series due to computational time/resources and observations that will be explained in the following chapters.

Table 3.6: Parameter tuning test matrix

Test #	Subcutaneous Tissue	Skin	Bone	Nail
1	Viscoelastic and elastic ($r = 1/2$)	Linear elastic (E = 2 MPa, ν = 0.3)	Linear elastic (E = 17 GPa, ν = 0.3)	Linear elastic (E = 170 MPa, ν = 0.3)
2	Viscoelastic and elastic ($r = 1/4$)	Linear elastic (E = 2 MPa, ν = 0.3)	Linear elastic (E = 17 GPa, ν = 0.3)	Linear elastic (E = 170 MPa, ν = 0.3)
3	Viscoelastic and elastic ($r = 1/8$)	Linear elastic (E = 2 MPa, ν = 0.3)	Linear elastic (E = 17 GPa, ν = 0.3)	Linear elastic (E = 170 MPa, ν = 0.3)
4	Viscoelastic and elastic ($r = 1/4$)	Elastic Lamina (Tonge 2013 [47])	Linear elastic (E = 17 GPa, ν = 0.3)	Linear elastic (E = 170 MPa, ν = 0.3)
5	Viscoelastic and elastic ($r = 1/8$)	Elastic Lamina (Tonge 2013 [47])	Linear elastic (E = 17 GPa, ν = 0.3)	Linear elastic (E = 170 MPa, ν = 0.3)
6	Viscoelastic and elastic ($r = 1/16$)	Elastic Lamina (Tonge 2013 [47])	Linear elastic (E = 17 GPa, ν = 0.3)	Linear elastic (E = 170 MPa, ν = 0.3)

4

Results

4.1 Geometry

The resulting final geometry as shown in Figure 4.1b has a more realistic skeletal structure as compared to the original (Figure 4.1a).

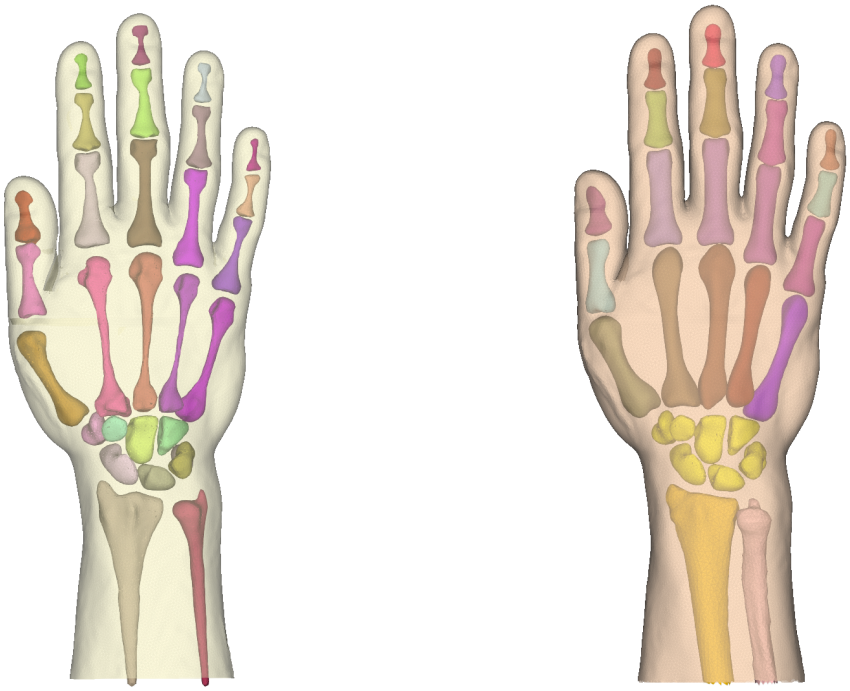

(a) Original geometry **(b)** Final geometry

Figure 4.1: Comparison of original and final hand model geometry

4.2 Model development

Both hexahedral and tetrahedral meshed models are shown in Figure 4.2, where the hexahedral model has some geometrical simplifications such as skin texture and roundness of bone ends as compared to the very realistic looking tetrahedral model. This can be associated to the hexablock fitting which could be further developed with time and choice of mesh resolution.

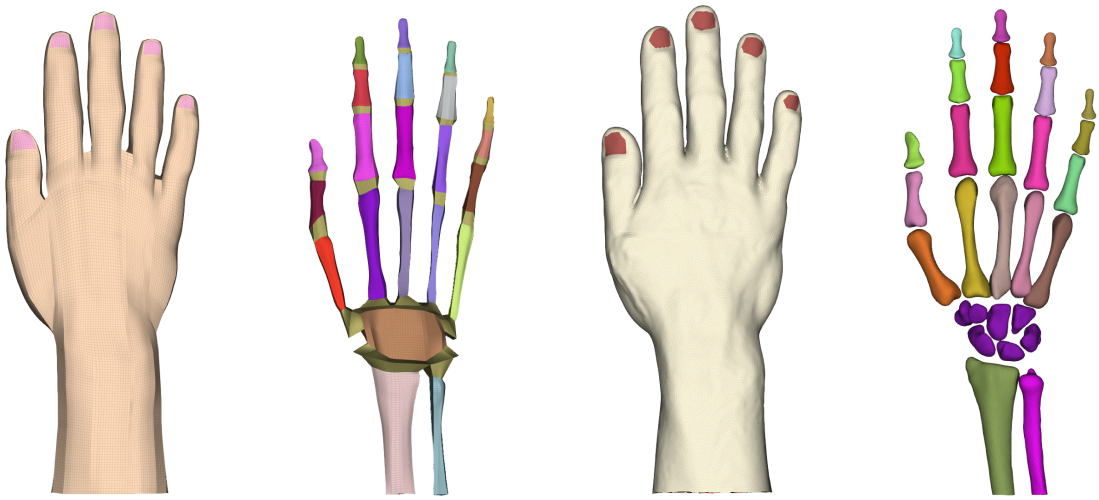

(a) Full hand hexahedral mesh model

(b) Hexahedral mesh of hand skeleton

(c) Full hand tetrahedral mesh model

(d) Tetrahedral mesh of hand skeleton

Figure 4.2: Comparison of hexahedral and tetrahedral mesh models

The number of elements for each model is as follows: total number of elements in hexahedral model is 584 184, with 29 544 shell elements and 554 640 solid elements; total number of elements in tetrahedral model is 1 312 762, with 60 948 shell elements and 1 251 814 solid elements. The breakdown of element type and element number per PID for each model is shown in Table 4.4 and Table 4.2, for hexahedral and tetrahedral models respectively. It can be noted that the tetrahedral model uses more than double the amount of elements than the hexahedral model. Additionally, although the skin and nails are shells, they were given a thickness of 1.2 mm [42],[43],[41] and 0.6 mm [45] respectively, based off of the model in [1].

4.3 Material Model Selection

After the first 3 parameter tuning simulations (see Table 3.6 for test matrix), the resulting fingertip force is as seen in Figure 4.3. The shape follows the expected curve, however, the magnitude is 3 to 10 times higher than the experimental data. Additionally, we see that the lowest stiffness case ($r = 1/8$) produced a significantly stiffer response than the other more stiff cases which is not correct. From these observations, it was decided to change the skin material model from linear elastic to elastic lamina and investigate if the model response stiffness could be further reduced.

New simulations were run and the first resulting curve can be seen in Figure 4.4b, curve labelled r=1/4 v1. In this simulation, we achieved a much more realistic response as compared to the experimental curve (labelled 0.3 mm/s), but the response was still too stiff. However, upon closer inspection of the visual simulation output, it was noted that the indenter plates starting position was not above the finger but rather compressing the fingertip a little bit and the finger pulp curvature was too

Table 4.1: Hexahedral

PID	Name	Element type	# of Elements
1000	SOFT-Hand-Skin	Shell-Quadrilateral	29 184
1001	SOFT-Subcutaneous-Tissue	Solid-Hexahedral	415 056
1002	BONE-Radius	Solid-Hexahedral	16 224
1003	BONE-Ulna	Solid-Hexahedral	8 736
1004	BONE-Carpals	Solid-Hexahedral	12 672
1005	BONE-Metacarpal-1	Solid-Hexahedral	5 184
1006	BONE-Metacarpal-2	Solid-Hexahedral	5 184
1007	BONE-Metacarpal-3	Solid-Hexahedral	5 184
1008	BONE-Metacarpal-4	Solid-Hexahedral	5 184
1009	BONE-Metacarpal-5	Solid-Hexahedral	5 184
1010	BONE-Proximal-Phalanx-1	Solid-Hexahedral	2 304
1011	BONE-Proximal-Phalanx-2	Solid-Hexahedral	4 032
1012	BONE-Proximal-Phalanx-3	Solid-Hexahedral	4 032
1013	BONE-Proximal-Phalanx-4	Solid-Hexahedral	4 032
1014	BONE-Proximal-Phalanx-5	Solid-Hexahedral	2 880
1015	BONE-Middle-Phalanx-2	Solid-Hexahedral	2 304
1016	BONE-Middle-Phalanx-3	Solid-Hexahedral	2 880
1017	BONE-Middle-Phalanx-4	Solid-Hexahedral	3 168
1018	BONE-Middle-Phalanx-5	Solid-Hexahedral	2 304
1019	BONE-Distal-Phalanx-1	Solid-Hexahedral	2 880
1020	BONE-Distal-Phalanx-2	Solid-Hexahedral	2 880
1021	BONE-Distal-Phalanx-3	Solid-Hexahedral	2 880
1022	BONE-Distal-Phalanx-4	Solid-Hexahedral	2 880
1023	BONE-Distal-Phalanx-5	Solid-Hexahedral	2 880
1024	NAIL	Shell-Quadrilateral	360

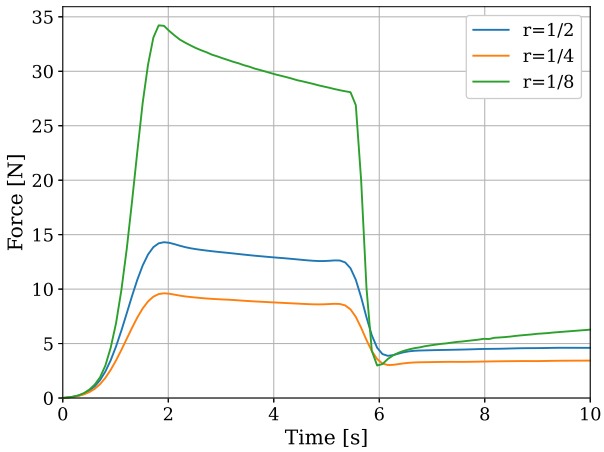

Figure 4.3: Simulation results for tests 1 through 3 for Series B loading case

Table 4.2: Tetrahedral

PID	Name	Element type	# of Elements
1000	SOFT-Hand-Skin	Shell-Triangular	60 277
1001	SOFT-Subcutaneous-Tissue	Solid-Tetrahedral	944 554
1002	BONE-Radius	Solid-Tetrahedral	18 017
1003	BONE-Ulna	Solid-Tetrahedral	9 292
1004	BONE-Carpals	Solid-Tetrahedral	22 944
1005	BONE-Metacarpal-1	Solid-Tetrahedral	21 327
1006	BONE-Metacarpal-2	Solid-Tetrahedral	27 732
1007	BONE-Metacarpal-3	Solid-Tetrahedral	24 239
1008	BONE-Metacarpal-4	Solid-Tetrahedral	16 198
1009	BONE-Metacarpal-5	Solid-Tetrahedral	16 345
1010	BONE-Proximal-Phalanx-1	Solid-Tetrahedral	9 964
1011	BONE-Proximal-Phalanx-2	Solid-Tetrahedral	19 798
1012	BONE-Proximal-Phalanx-3	Solid-Tetrahedral	22 941
1013	BONE-Proximal-Phalanx-4	Solid-Tetrahedral	19 838
1014	BONE-Proximal-Phalanx-5	Solid-Tetrahedral	12 777
1015	BONE-Middle-Phalanx-2	Solid-Tetrahedral	10 435
1016	BONE-Middle-Phalanx-3	Solid-Tetrahedral	12 341
1017	BONE-Middle-Phalanx-4	Solid-Tetrahedral	9 789
1018	BONE-Middle-Phalanx-5	Solid-Tetrahedral	7 681
1019	BONE-Distal-Phalanx-1	Solid-Tetrahedral	5 134
1020	BONE-Distal-Phalanx-2	Solid-Tetrahedral	5 016
1021	BONE-Distal-Phalanx-3	Solid-Tetrahedral	5 526
1022	BONE-Distal-Phalanx-4	Solid-Tetrahedral	5 444
1023	BONE-Distal-Phalanx-5	Solid-Tetrahedral	4 482
1024	NAIL	Shell-Triangular	671

flat. These 2 points will be shown and investigated in more detail in the next section but the corresponding adjustments were made and this time both series of data were simulated. The resulting force-displacement curves are shown in Figure 4.4, where we get a less stiff model response when reducing the material stiffness and better fingertip responses.

An additional simulation was conducted with the tetrahedral model to compare the response against the hexahedral model. The exact same test case was setup for both models and Figure 4.5 shows the result. As can be seen, the response from both models is almost identical, with only a very small stiffness increase in some areas for the tetrahedral model in comparison with the hexahedral model.

The nail and bone material models were kept the same for all simulations, so only variations for skin and subcutaneous tissue were considered when choosing the tuning parameters for a baseline model. Primarily from visual observations from Figure 4.4, a baseline material choice was selected as outlined in Table 4.3. This choice will be further defended in section 4.5 with the calculation of the CORA score.

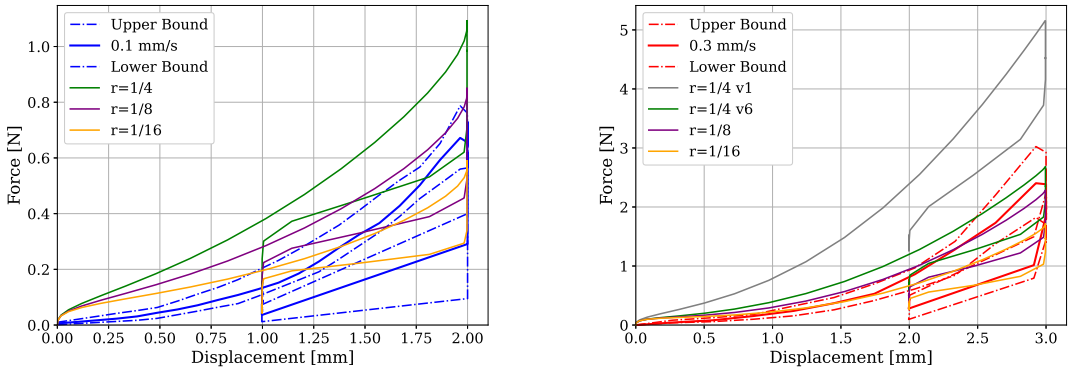

(a) Series A **(b)** Series B

Figure 4.4: Simulation results for tests 4 through 6 for both series of loading cases

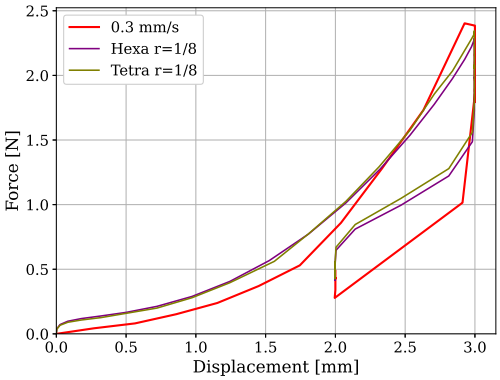

Figure 4.5: Hexahedral versus tetrahedral simulation output for series B and polynomial soft-tissue stiffness of 1/8

Table 4.3: Baseline material model choice

Subcutaneous Tissue	**Skin**	**Bone**	**Nail**
Viscoelastic and elastic ($r = 1/8$)	Elastic Lamina	Linear elastic (E = 17 GPa, ν = 0.3)	Linear elastic (E = 170 MPa, ν = 0.3)

4.4 Joint Kinematics and Positioning

Initial attempts to position the baseline hexahedral hand model into a pinch grip were conducted without the implemented joint model. Rather, a displacement induced "pulling" of the fingers into the desired location was used. This however did not work as expected and therefore two additional model geometries were created, where the problematic area, the thumb, was repositioned before the repositioning simulations were attempted. The models are shown in Figure A.1, and Figure A.2, Figure A.3

for model versions 2 and 3 respectively. The implemented kinematic joints (baseline model) were not fully tested, so no analysis if the joint movement was indeed biofidelic can be conducted.

4.5 Model feasibility: experiments and simulations

Based on the observations made in section 4.3, the initial and corrected simulation setup can be viewed in Figure 4.6. In addition to the finger pulp geometry changes and indenter starting position, the final compressed displacement needed to be adjusted. In Figure 4.7, in the initial model, the vertical displacement overshot 3 mm ($\sim$ 3.3 mm or sometimes undershot at roughly 2.7 mm) and had a much larger off-center compressed area as compared to the corrected model.

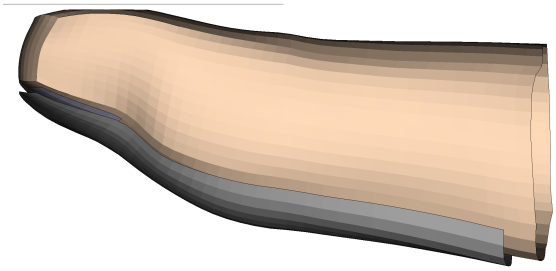

(a) Initial setup side view

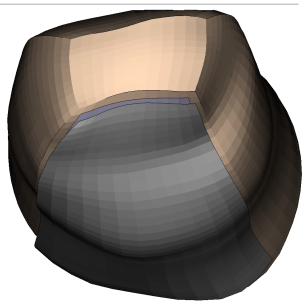

(b) Initial setup front view

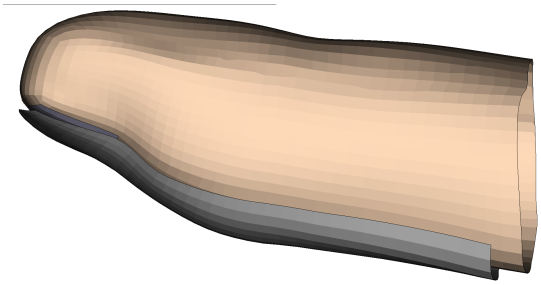

(c) Updated setup side view

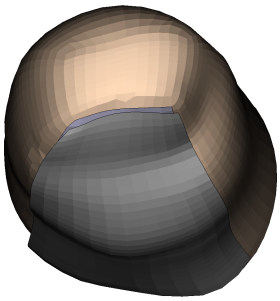

(d) Updated setup front view

Figure 4.6: Simulation setup for compressive fingertip tests, where subplots a) and b) show the initial version setup with flat finger geometry and compressing indenter starting position. Subplots c) and d) show the fixed simulation setup with rounded finger pulp geometry and non touching indenter position.

A comparison of the Von Mises stress among the two model types at different time steps is shown in Figure 4.8 (for simplicity, the Hexahedral model is referred to as Hexa, and the Tetrahedral model is referred to as Tetra). From the visual comparison, it can be seen that both models have similar areas of stress but the tetrahedral model has an additional area of high stress at the nail tip.

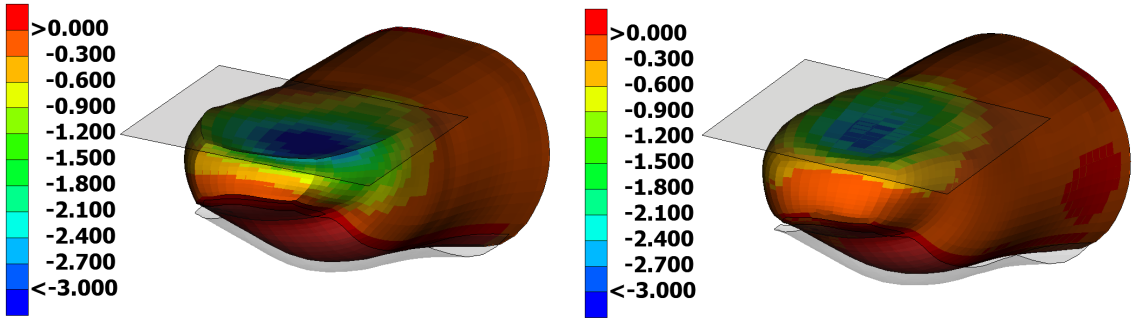

(a) Initial setup full compression fringe **(b)** Updated setup full compression fringe

Figure 4.7: Vertical displacement fringe plot for initial and updated simulation setups for series B at max compression (3 mm)

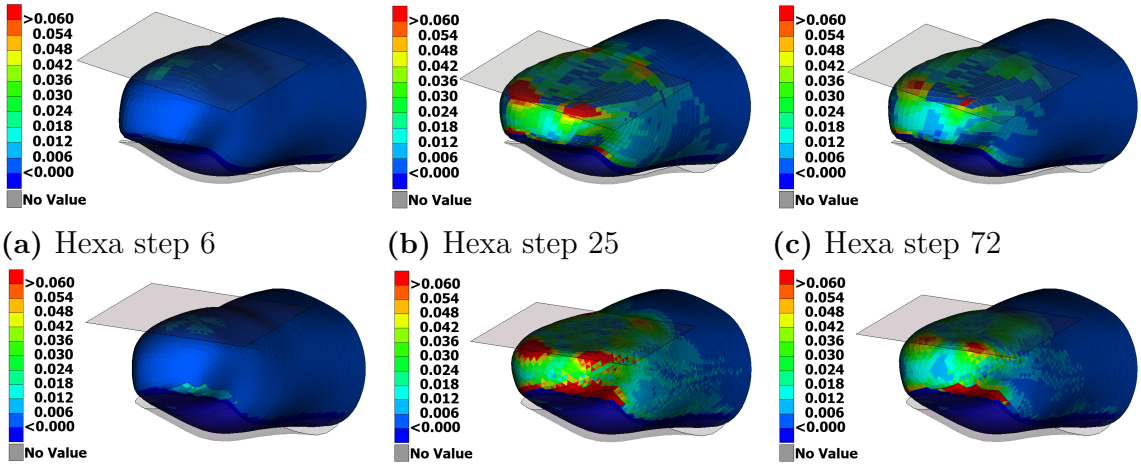

(a) Hexa step 6 **(b)** Hexa step 25 **(c)** Hexa step 72

(d) Tetra step 6 **(e)** Tetra step 25 **(f)** Tetra step 72

Figure 4.8: Von Mises stress comparison for hexahedral and tetrahedral models with soft-tissue stiffness of $r = 1/8$ under the Series B loading case at three different time steps. Step 6 corresponds to the initial contact between the plate and fingertip, step 25 to the maximum fingertip compression at 3 mm displacement, and step 72 to the maximum fingertip compression at 2 mm displacement.

The CORA score was calculated for the first loading segment (i.e. up to first compression value, 2 mm or 3 mm for Series A and B respectively) for both models and for both series from the material tuning stage. The results are displayed in Table 4.4, where Series A is denoted by (A) and Series B is denoted by (B). The corridor and cross-correlation component weightings were both 0.5, with the corridor width set to 0.1. From the table, it can be noted that there is not one clear model that fits best to the experimental data. The parameter tuning shows that the material model with lowest elastic stiffness (1/16) best fits the series A loading case, however, the opposite is true for series B, where the highest stiffness (1/4) best fits the experimental data. Again, we see that there is no significant difference between the tetrahedral and hexahedral models when subjected to the same test case. Overall, it can be said that the 1/8 polynomial material model yields the most accurate

results for both series of experimental data.

Table 4.4: CORA score for curve comparison between various parameter tuning simulations and experimental data

Case	CORA score	Corridor comp.	Cross-corr. comp.	Classification
Poly 1/4 vs. mean (A)	0.5202	0.0500	0.9904	Acceptable
Poly 1/8 vs. mean (A)	0.5468	0.1000	0.9937	Acceptable
Poly 1/16 vs. mean (A)	0.8464	0.7000	0.9928	Good
Poly 1/16 vs. lower bound (A)	0.6708	0.3500	0.9916	Acceptable
Poly 1/4 vs. upper bound (A)	0.6480	0.3000	0.9959	Acceptable
Poly 1/4 vs. mean (B)	0.9691	0.9444	0.9938	Excellent
Poly 1/8 vs. mean (B)	0.8292	0.6667	0.9918	Good
Poly 1/16 vs. mean (B)	0.6345	0.2778	0.9912	Acceptable
Poly 1/16 vs. lower bound (B)	0.9706	0.9444	0.9967	Excellent
Poly 1/4 vs. upper bound (B)	0.6617	0.3333	0.9901	Acceptable
Tetra Poly 1/8 vs. mean (B)	0.8280	0.6667	0.9894	Good

5
Discussions

5.1 Geometry

Generally, what we see in Figure 4.1a, is that the bones are too skinny (e.g. the middle regions of the metacarpals) and the gaps between bones are too large. To increase the biofidelity, parts from other open source models that fit or could be adjusted to match the statistical average size were used. For the MRI scan used to derive the original geometry, the hand was placed on a pillow. This resulted in the curvature on the palmar side of the hand and orientation of the fingers to be affected, with the main issues arising around the thumb and thumb gap. An additional scan of the palmar side of the hand (not MRI) was used to measure the thumb gap and make the proper adjustments (i.e. remove some hexahedral elements) in the hexahedral model. This scan was also used to adjust the curvature of the fingers, especially the finger pulp in the hexahedral model, as this was the main focus of the simulations.

5.2 Model development

The hexablock fitting of the outer skin went smoothly, but when moving in to the bones with the o-grids, challenges arose. In order to keep good box/mesh quality, many bones became shorter and skinnier (e.g. metacarpals 3-5 had significant reduction in thickness and changed angle of orientation), working against some efforts made in the geometry stage. This is in part due to the overall approach of fitting the bones and hexablocks, which could be further refined with additional effort and time. This model provides good morphing capabilities, however further refinement would be beneficial to reduce the risk of unwanted errors due to some poorly shaped and fitted boxes.

The tetrahedral model was much simpler to mesh due to the automatic process and maintained the corrected geometry with only one non-biofidelic area being the nails. The nails had to be manually selected from the skin shell and the shape/orientation of the triangular elements did not always make the selection ideal or realistic looking. The influence of this showed up in the stress analysis (Figure 4.8) where the tetrahedral model had an additional area of high stress at the corner of the nail as compared to the hexahedral model. The tetrahedral model also has over double the amount of elements with respect to the hexahedral model, this increases the computational cost and difficulty to converge. These disadvantages further support the choice for the hexahedral model as the baseline.

5.3 Material model selection

From the simulation results, there is no material model that matches the experimental curve or stays within the experimental bounds. Directly from the beginning, the simulation has a sharp stiffness response that levels off before reversing to slope up unlike the experimental data, which starts off with a very slow increase in force before it starts to slope much steeper with increasing displacement. This difference could be attributed to the simulation setup and not knowing what the authors in [6] took as the start of their experimental data. We assume it to be the start of the contact between the indenter and the fingertip but some discrepancy can be introduced from this assumption between the experimental and simulated data.
Overall, the material model tuning is still a bit too stiff and further testing should be conducted. Our response has the viscous part being too small and the elastic component being too big. For further testing, the elastic component should be tuned to match the lowest strain rate, and then the viscous component should be tuned to match the highest strain rate. Retuning is one option if the exact loading case is known. Otherwise, retuning would not facilitate variability in future tests and since we don't know the exact loading rate, the results could be completely wrong. Therefore, a better option is to validate the model and parameters. In order to validate the material model, an additional dataset(s) would be required. This would ensure that one dataset could be used for tuning the parameters and the other(s) for validating and assessing the biofidelity.

5.4 Joint kinematics

More simulations and work is needed to ensure biofidelic joint movement to reposition the hand. As previously mentioned, the thumb is a problematic area and this introduces orientational challenges when trying to reposition the hand into another position, such as a precision pinch grip. The creation of additional models did not help this issue, so the kinematic joints could be tested to see if they can lead to a viable solution.

5.5 Model feasibility: experiments and simulations

For our simulation setup, we created the finger holder from the dorsal profile of the index finger. The index finger was directly taken from the full hand model and if observed closely, the finger is not oriented symmetrically (slightly rotated) under the indenter plate. This is a potential discrepancy in comparison to the experimental setup and can introduce an uneven response in the simulation results. Due to the nail's manually selected structure and finger orientation, an uneven model response is clearly shown in the Von Mises stress response of the tetrahedral model in Figure 4.8. There, it can be noticed that a large stress is present at one corner of the nail that is not present on the other side. More evidence of this finger orientation is shown in

Figure 4.7a, where the largest compression is concentrated in one corner/side of the fingertip. This however was improved when the finger pulp curvature was adjusted as is seen in Figure 4.7b, where the largest compression is now in the middle, with a more even response around it.
From the parameter tuning tests (tests 4-6), the CORA score is calculated with respect to the experimental mean curve and to the experimental bounds (both for the respective series simulated). Overall, the bounds (stiffness 1/4 to upper bound and stiffness 1/16 for lower bound) have quite high scores for both series, but simulation results with respect to the average experimental data is a bit mixed. It can be concluded that the 1/8 polynomial material model yields the most accurate results for both series, however, this is with acceptable and quite low CORA scores. Ideally, the scores would be higher for both series with one clear match, therefore more variation in material models should still be investigated. On another note, the tetrahedral model showed almost identical CORA score values to the hexahedral model, so in terms of the vertical force response (input to CORA function), there is no clear model that is significantly better.

5.6 Generalization and contributions

The developed model, although not fully biofidelic at this stage, can be used for comparative studies looking into ergonomic product simulations. More specifically, if there is a desire to compare various products or ideas, this model can be used for such an analysis rather than for observing precise biological responses. For morphing, target sizes or dimensions are needed along with a mesh morphing software. This model can provide insight into tissue stresses not visible or measurable in conventional experiments and provide valuable insight into the comfort of products not investigated previously.
In the end, a new average anatomical FE human hand model for comfort analysis has been created. It provides insight into geometry and meshing considerations, parameter tuning for material model selection, and kinematic joint implementation.

6
Conclusion

Medtech companies are essential players in the healthcare setting and the need to improve and investigate their products for ergonomics and comfort is essential. This thesis outlined the necessary steps to develop and tune an average human hand FE model for applications in MedTech product research and development.
Development started with choosing a target size, this was taken as the statistical average from a human population dataset. An original model based off of an MRI scan matching the target size was taken as the starting point. However, due to some biofidelic issues in the bone shape and spacing, some open source models were investigated. After lots of model measurements, two models, OpenHands and PIPER reference were selected, where some bones from these models were either morphed and/or replaced into the original model. The original skin was kept the same but adjustments to the skin curvature (mainly fingertips) and thumb gap were conducted on the meshed model.
Two versions of the model were created, a hexahedral and a tetrahedral, with the main meshing process comprised of fitting hexablocks to the geometry. It was conducted in an outside-in approach, where first the skin was fitted and then the bones were fitted with o-grids. This lead to the hexahedral model and the tetrahedral model was generated automatically. From the simulation results, there was practically no difference in the force response between the two models, but when comparing the Von Mises stress, the tetrahedral model showed an additional area of high stress at one corner of the nail. This difference can be attributed to the orientation of the finger and/or manual selection of the nail elements. Additionally, the tetrahedral model has over double the amount of elements as compared to the hexahedral model and can have the potential to experience difficulties converging. Therefore, the hexahedral model was chosen as the baseline and also for its morphing capabilities.
Material models were taken from published sources along with the experimental setup for a slow loading rate fingertip compressive test. Many combinations and iterations were conducted, with a baseline choice consisting of viscoelastic with stiffness ratio of 1/8 (elastic component) for the subcutaneous tissue, elastic lamina for the skin and linear elastic (rigid) for the bones and nails. The material model is however not validated as an additional dataset is required.
A kinematic joint model using local coordinate systems, rigid wires, and torsional springs was implemented in the finger joints (DIP, PIP, MCP). Successful biofidelic repositioning of the hand into a precision pinch grip was not successful and needs further investigation.
Overall, the model can be used for comparative simulation studies and has been chosen with morphing capabilities in mind.

6.1 Future Work

Conduct in house validation tests due to the lack of available published data. This can consist of compressive tests with low loading rate for fingertips (or regions across the full hand) to validate the material models. Along with this, more variations in material models should be investigated. Further refinement of the mesh in the hexahedral model would be beneficial before moving on to any morphing software or simulation with products. Additionally, more simulations of hand repositioning needs to be investigated to ensure biofidelic movement and capabilities of the hand model.

Bibliography

[1] J. Z. Wu, D. E. Welcome, and R. G. Dong, "Three-dimensional finite element simulations of the mechanical response of the fingertip to static and dynamic compressions," *Computer Methods in Biomechanics and Biomedical Engineering*, vol. 9, pp. 55–63, 2006.

[2] M. R. V. (LadyofHats) and Nyks, "Scheme human hand bones-en." `https://commons.wikimedia.org/wiki/File:Scheme_human_hand_bones-en.svg`, 2007. Public domain image released by the author on Wikimedia Commons.

[3] CCCOnline, *Skeletal Structures and Functions*. CCCOnline Pressbooks, 2020. Accessed: 2026-01-02.

[4] OpenClipart contributor, "Human hand palm inside remix." `https://freesvg.org/human-hand-palm-inside-remix`, 11 2019. Public Domain (CC0) license. SVG ID: 174027.

[5] Y. Wei, Z. Zou, Z. Qian, L. Ren, and G. Wei, "Biomechanical analysis of the effect of finger joint configuration on hand grasping performance: Rigid vs flexible," *IEEE Transactions on Neural Systems and Rehabilitation Engineering*, vol. 31, pp. 606–619, 2023.

[6] J. Z. Wu, R. G. Dong, W. P. Smutz, and S. Rakheja, "Dynamic interaction between a fingerpad and a flat surface: Experiments and analysis," *Medical Engineering and Physics*, vol. 25, pp. 397–406, 2003.

[7] P. Mylon, R. Lewis, M. J. Carré, N. Martin, and S. Brown, "A study of clinicians' views on medical gloves and their effect on manual performance," *American Journal of Infection Control*, vol. 42, pp. 48–54, 1 2014.

[8] Z. Wang, Y. Qiu, X. Zheng, Z. Hao, and C. Liu, "Biomechanical models of the hand-arm system to predict the hand gripping forces and transmitted vibration," *International Journal of Industrial Ergonomics*, vol. 88, 3 2022.

[9] G. HARIH and M. TADA, "Development of a finite element digital human hand model," pp. 208–213, Hometrica Consulting, 11 2016.

[10] Y. Wei, Z. Zou, G. Wei, L. Ren, and Z. Qian, "Subject-specific finite element modelling of the human hand complex: Muscle-driven simulations and experimental validation," *Annals of Biomedical Engineering*, vol. 48, pp. 1181–1195, 4 2020.

[11] Y. Zhang, H. Xie, and M. J. Lake, "Accuracy prediction of wearable flexible smart gloves," *Autex Research Journal*, vol. 24, 1 2024.

[12] A. Yu, K. L. Yick, S. P. Ng, J. Yip, and Y. F. Chan, "Numerical simulation of pressure therapy glove by using finite element method," *Burns*, vol. 42, pp. 141–151, 2016.

[13] I. Albrecht, J. Haber, and H.-P. Seidel, "Construction and animation of anatomically based human hand models," tech. rep., Eurographics/SIGGRAPH Symposium on Computer Animation, 2003.

[14] A. Kumar, T. S. Mundra, and A. Kumar, *Anatomy of Hand*, pp. 28–35. Boston, MA: Springer US, 2009.

[15] C. L. Taylor and R. J. Schwarz, "The anatomy and mechanics of the human hand," *Artificial Limbs*, vol. 2, pp. 22–35, 1955.

[16] J. Iraeus, "Cae crash simulation theory," 2025. Lecture slides, TME202 - Vehicle Traffic Safety course.

[17] C. Obbink-Huizer, "Implicit vs explicit finite element analysis: When to use which," 2023. Accessed: 2025-10-20.

[18] A. Putra, "Human body material tissue library: Internal technical report," internal technical report, ALTEN, August 2022. Confidential internal report.

[19] G. Cei, A. Artoni, and M. Bianchi, "A review on finite element modelling of finger and hand mechanical behaviour in haptic interactions," *Biomechanics and Modeling in Mechanobiology*, vol. 24, pp. 895–917, 6 2025.

[20] G. Harih and M. Tada, *Development of a feasible finite element digital human hand model*, pp. 273–286. Elsevier, 1 2019.

[21] G. Harih, M. Kalc, M. Vogrin, and M. Fodor-Mühldorfer, "Finite element human hand model: Validation and ergonomic considerations," *International Journal of Industrial Ergonomics*, vol. 85, 9 2021.

[22] L. Modenese, "Awesome biomechanics." `https://github.com/modenaxe/awesome-biomechanics`, 2020. Accessed section: Finite Element Models. Repository created 2020-08-14.

[23] J. John, C. Klug, M. Kranjec, E. Svenning, and J. Iraeus, "Hello, world! viva+: A human body model lineup to evaluate sex-differences in crash protection," *Frontiers in Bioengineering and Biotechnology*, vol. 10, 2022. Webpage available at: `https://vivaplus.readthedocs.io/en/latest/`.

[24] "start [piper-project.org]." `http://www.piper-project.org/start`, 2025. Related resources: Piper github; `https://gitlab.com/piper-project.org`, Piper reference model github; `https://gitlab.com/piper-project.org/misc_models/-/tree/master/registration_reference_model`.

[25] Toyota Motor Corporation, "Thums: Total human model for safety." `https://www.toyota.co.jp/thums/`, 2025. Official THUMS information page.

[26] IT'IS Foundation, "Virtual population overview." `https://itis.swiss/virtual-population/virtual-population/overview/`, 2025. Overview of the Virtual Population (ViP) anatomical models.

[27] T. A. Munyebvu, C. D. Metcalf, C. B. Burson-Thomas, D. Warwick, C. Everitt, L. King, A. Darekar, M. Browne, M. O. Heller, and A. S. Dickinson, "Openhands: An open-source statistical shape model of the finger bones," *Annals of Biomedical Engineering*, vol. 52, pp. 2975–2986, 11 2024. Github available at: `https://github.com/abel-research/OpenHands`.

[28] T. Mäki and H. Lauvdal, "Modelling of the simplified and anatomical hand: Part a," Technical Report Revision 1, Mölnlycke Health Care, September 2024. MHC Internal.

[29] M. T. Diaz, A. R. Benoit, K. M. Kearney, T. F. Kelly, E. M. Lindbeck, I. Tappan, W. S. Bowers, L. Durai, J. B. Nunag, M. B. Officer, J. B. Harley, and J. A. Nichols, "A hand biomechanics dataset of kinematics, kinetics, electromyography, and imaging in healthy adults," 8 2025.

[30] M. Mirakhorlo, J. M. Visser, B. A. G. de Monsabert, F. C. van der Helm, H. Maas, and H. E. Veeger, "Anatomical parameters for musculoskeletal modeling of the hand and wrist," *International Biomechanics*, vol. 3, pp. 40–49, 2016.

[31] D. N. Rocha, R. N. Jorge, and M. Pinotti, "Development of 3d biomechanical model of the human hand using fem," 2009.

[32] N. J. Jarque-Bou, M. Atzori, and H. Müller, "A large calibrated database of hand movements and grasps kinematics," *Scientific Data*, vol. 7, 12 2020.

[33] C. Thunert, *CORAplus 4.1.0 User's Manual*. GNS mbH on behalf of PDB – Partnership for Dummy Technology and Biomechanics, Braunschweig, Germany, 2023. Version 4.1.0.

[34] OpenClipart contributor, "Cube." `https://freesvg.org/1511013198`, 06 2021. Public Domain (CC0) license. SVG ID: 177941.

[35] OpenClipart contributor, "Tetraedre." `https://freesvg.org/tetraedre`, 06 2021. Public Domain (CC0) license. SVG ID: 178112.

[36] G. Harih and B. Dolšak, "Recommendations for tool-handle material choice based on finite element analysis," *Applied Ergonomics*, vol. 45, pp. 577–585, 2014.

[37] E. R. Serina, C. D. Mote, and D. Rempelts, "Force response of the fingertip pulp to repeated compression-effects of loading rate, loading angle and anthropometry," *Journal of Biomechanics*, vol. 30, pp. 1035–1040, 1997.

[38] A. Ali, M. Hosseini, and B. B. Sahari, "A review of constitutive models for rubber-like materials," *American Journal of Engineering and Applied Sciences*, vol. 3, pp. 232–239, Mar 2010.

[39] J. Z. Wu, R. G. Dong, S. Rakheja, and A. W. Schopper, "Simulation of mechanical responses of fingertip to dynamic loading," *Medical Engineering & Physics*, vol. 24, no. 4, pp. 253–264, 2002.

[40] L. Pan, L. Zan, and F. Foster, "Ultrasonic and viscoelastic properties of skin under transverse mechanical stress in vitro," *Ultrasound in Medicine Biology*, vol. 24, no. 7, pp. 995–1007, 1998.

[41] P. Agache, "Main skin physical constants," in *Measuring the Skin* (P. Agache and P. Humbert, eds.), pp. 747–757, Berlin, Heidelberg: Springer-Verlag, 2004.

[42] F. M. Hendriks, D. Brokken, J. T. van Eemeren, C. W. Oomens, F. P. Baaijens, and J. B. Horsten, "A numerical-experimental method to characterize the non-linear mechanical behavior of human skin," *Skin Research and Technology*, vol. 9, pp. 274–283, 8 2003.

[43] F. M. Hendriks, D. Brokken, C. W. Oomens, and F. P. Baaijens, "Influence of hydration and experimental length scale on the mechanical response of human skin *in vivo*, using optical coherence tomography," *Skin Research and Technology*, vol. 10, no. 4, pp. 231–241, 2004.

[44] H. Yamada and F. Evans, *Strength of Biological Materials*. Williams & Wilkins, 1970.

[45] R. Baran, "Nail anatomy and physiology," in *Measuring the Skin* (P. Agache and P. Humbert, eds.), pp. 290–293, Berlin, Heidelberg: Springer-Verlag, 2004.

[46] J. Z. Wu, R. G. Dong, W. P. Smutz, and A. W. Schopper, "Modeling of time-dependent force response of fingertip to dynamic loading," *Journal of Biomechanics*, vol. 36, pp. 383–392, 3 2003.

[47] T. K. Tonge, L. S. Atlan, L. M. Voo, and T. D. Nguyen, "Full-field bulge test for planar anisotropic tissues: Part i-experimental methods applied to human skin tissue," *Acta Biomaterialia*, vol. 9, pp. 5913–5925, 2013.

[48] N. W. Tschoegl, *The phenomenological theory of linear viscoelastic behavior: an introduction*. New York: Springer-Verlag, 1989.

A

Appendix 1

A.1 Meshing

Table A.1: Detailed component identifiers and naming

Component Identifier	Name
1000	SOFT-Hand-Skin
1001	SOFT-Subcutaneous-Tissue
1002	BONE-Radius
1003	BONE-Ulna
1004	BONE-Carpals
1005	BONE-Metacarpal-1
1006	BONE-Metacarpal-2
1007	BONE-Metacarpal-3
1008	BONE-Metacarpal-4
1009	BONE-Metacarpal-5
1010	BONE-Proximal-Phalanx-1
1011	BONE-Proximal-Phalanx-2
1012	BONE-Proximal-Phalanx-3
1013	BONE-Proximal-Phalanx-4
1014	BONE-Proximal-Phalanx-5
1015	BONE-Middle-Phalanx-2
1016	BONE-Middle-Phalanx-3
1017	BONE-Middle-Phalanx-4
1018	BONE-Middle-Phalanx-5
1019	BONE-Distal-Phalanx-1
1020	BONE-Distal-Phalanx-2
1021	BONE-Distal-Phalanx-3
1022	BONE-Distal-Phalanx-4
1023	BONE-Distal-Phalanx-5
1024	NAIL

A.2 Material Models

A.2.1 Material models from Wu et al. 2006 [1]

From [1], the derivation of their material models are as follows:
The constitutive equations used for the inner skin and subcutaneous tissue are somewhat comparative to the ones used in [46], where the total tissue stress ($\tilde{\sigma}$) is assumed to be comprised of elastic ($\tilde{\sigma}^0$) and viscous ($\tilde{\sigma}^v$) stress components. The relationship then follows as,

$$\tilde{\sigma}(t) = \tilde{\sigma}^0(t) + \tilde{\sigma}^v(t) = \tilde{\sigma}^0(t) + \int_0^t \frac{\dot{G}(\tau)}{G_0}\tilde{\sigma}^0(t-\tau)\,d\tau, \tag{A.1}$$

$$= \tilde{\sigma}^0(t) + \int_0^t \dot{g}(\tau)\tilde{\sigma}^0(t-\tau)\,d\tau, \tag{A.2}$$

where t is time. Next, the stress relaxation function can be defined using the Prony series ([48]) as,

$$g(t) = \frac{G(t)}{G_0} = \left[1 - \sum_{i=1}^{N_G} g_i \left(1 - e^{-\frac{t}{\tau_i}}\right)\right], \tag{A.3}$$

where G_0 and $G(t)$ are the instantaneous and time-dependent moduli, respectively, g_i and τ_i $(i = 1, 2, \ldots, N_G)$ are stress relaxation parameters, and N_G is the number of terms used in the stress relaxation function.
Additionally, a polynomial model is used to describe the elastic deformation of the inner skin and subcutaneous tissues which is defined as follows using a function of strain energy density per unit volume,

$$U = \sum_{i+j=1}^{N} C_{ij}\,(\,\bar{I}_1 - 3\,)^i\,(\,\bar{I}_2 - 3\,)^j + \sum_{i=1}^{N} \frac{1}{D_i}\,(J-1)^{2i}, \tag{A.4}$$

where $\bar{I}_1$ and $\bar{I}_2$ are the first and second deviatoric strain invariants, respectively, J is the elastic volume ratio, N, D_i, and C_{ij} are the material parameters.
For the parameters in the following two tables (Table A.2, Table A.3), which correspond to the inner skin were found by fitting the constitutive model Equation A.4 to the experimental data from [42], [43]. Additionally, the inner skin and subcutaneous tissue were both considered nearly incompressible.

Table A.2: Soft tissue viscoelastic parameters

Part	i	**1**	**2**
Inner skin	g_i	8.64e-2	2.14e-1
	τ_i (s)	2.12e-1	8.85e0
Subcutaneous tissue	g_i	2.57e-1	3.83e-1
	τ_i (s)	2.23e-1	4.68e0

For parameter values with stiffness ratios 1/8 and 1/16, the used values were slightly adjusted from the original values in Table A.3. This is to reflect observations that

the finger response becomes more stiff instead of less stiff for those stiffness ratios (in initial tests), so those parameters have been recalculated from the 1/4 values instead.

Table A.3: Soft tissue elastic parameters

Part (r is stiffness ratio)	C_{10}	C_{01}	C_{11}	C_{20}	C_{02}	D_1
Inner skin	2.34e-3	5.42e-3	-0.262	2.39e-1	7.47e-2	13.3
Subcutaneous tissue						
$r = 1/16$	1.49e-4	3.35e-4	-1.64e-2	1.49e-2	4.66e-3	13.3
$r = 1/8$	2.99e-4	6.70e-4	-3.28e-2	2.98e-2	9.35e-3	26.7
$r = 1/4$	5.97e-4	1.34e-3	-6.55e-2	5.96e-2	1.87e-2	53.3
$r = 1/2$	1.19e-3	2.70e-3	-1.31e-1	1.19e-1	3.73e-2	26.6

A.2.2 Ogden hyper-elastic material model

The Ogden strain energy potential ([38]) can be defined as follows,

$$U = \sum_{i=1}^{N} \frac{2\,\mu_i}{\alpha_i^2}\left[\bar{\lambda}_1^{\alpha_i} + \bar{\lambda}_2^{\alpha_i} + \bar{\lambda}_3^{\alpha_i} - 3 + \frac{1}{D_i}\Big(J_{\text{el}} - 1\Big)\right]^{2i}, \tag{A.5}$$

where $\bar{\lambda}_i$ are the deviatoric principal stretches, $\bar{\lambda}_i = J^{-1/3}\lambda_i$, λ_i are the principal stretches, N is the number of terms and μ_i, α_i are temperature-dependent material parameters that describe shear behaviour of the material, D_i is compressibility, J is the Jacobean determinant and J_{el} is the elastic volume ratio. For the Ogden model, the initial shear and bulk modulus are represented by,

$$\mu_0 = \sum_{i=1}^{N} \mu_i, \qquad K_0 = \frac{2}{D_1}. \tag{A.6}$$

Compressibility (defined as values less than 0.5 for the Poisson ratio) can be defined with the specified non-zero values for D_i, where,

$$D_i = \frac{2}{K_0} = \frac{3(1-2\nu)}{\mu_0(1+\nu)}. \tag{A.7}$$

The Ogden material model parameter values used for skin and subcutaneous tissue are summarized in Table A.4 and Table A.5 respectively.

Table A.4: Material parameters for Ogden material model for determining hyper-elasticity of skin

N	μ_i	α_i
1	-0.07594	4.941
2	0.01138	6.425
3	0.06572	4.712

Table A.5: Material parameters for Ogden material model for determining the hyper-elasticity of subcutaneous tissue

N	μ_i	α_i
1	-0.04895	5.511
2	0.00989	6.571
3	0.03964	5.262

A.3 Additional model variations

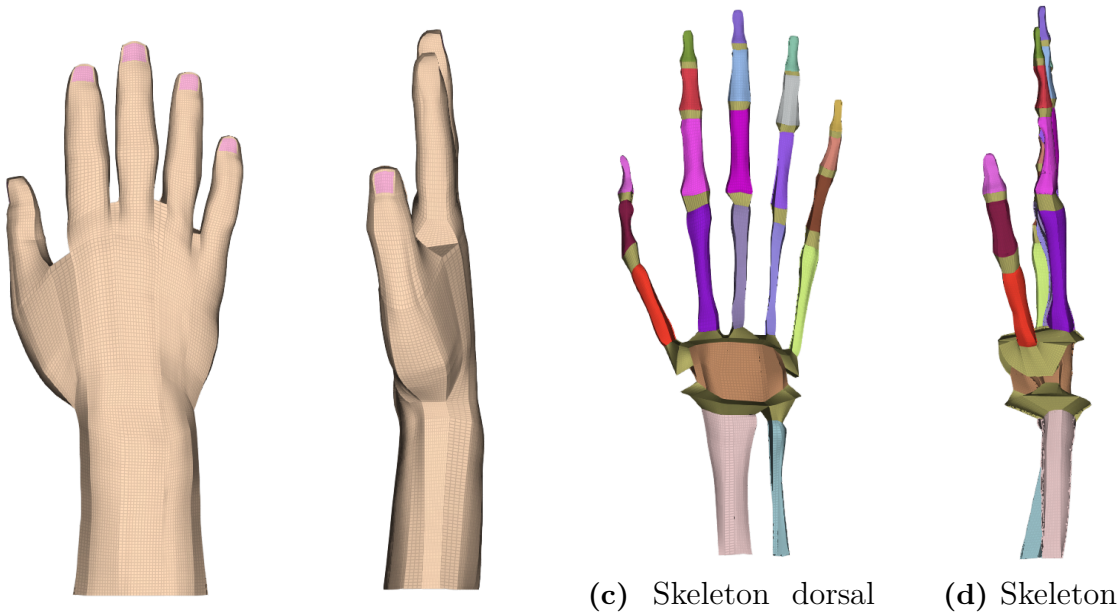

(a) Dorsal view **(b)** Side view **(c)** Skeleton dorsal view **(d)** Skeleton side view

Figure A.1: Meshed model and meshed skeleton for second thumb position model

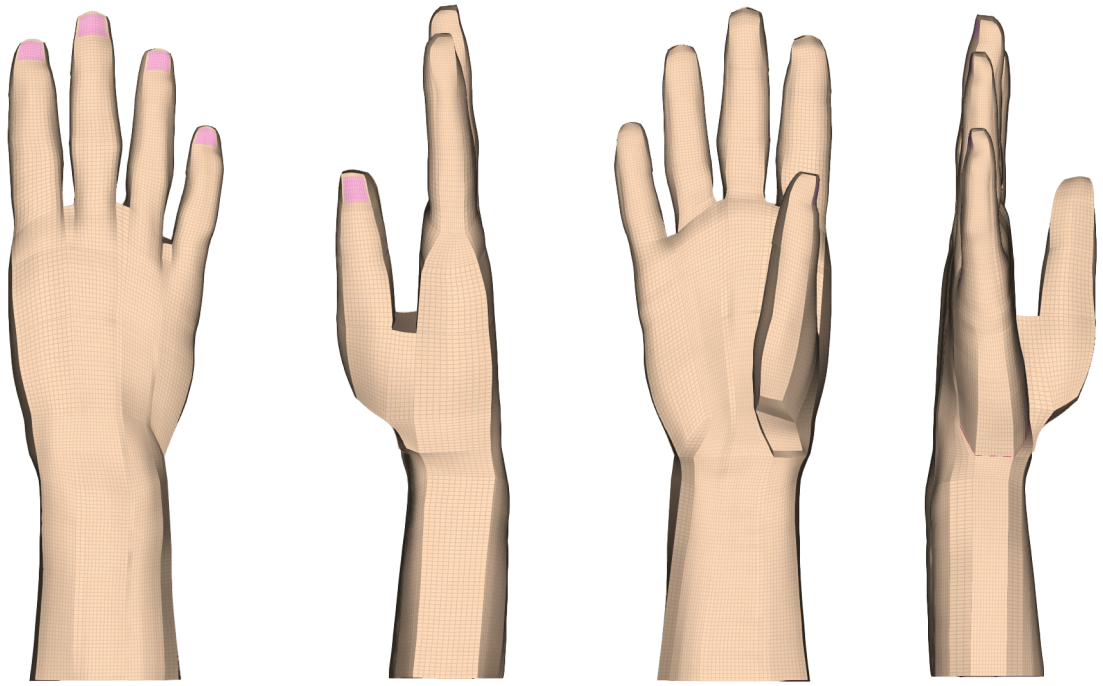

(a) Dorsal view **(b)** Side view 1 **(c)** Palmar view **(d)** Side view 2

Figure A.2: Meshed model for third thumb position model

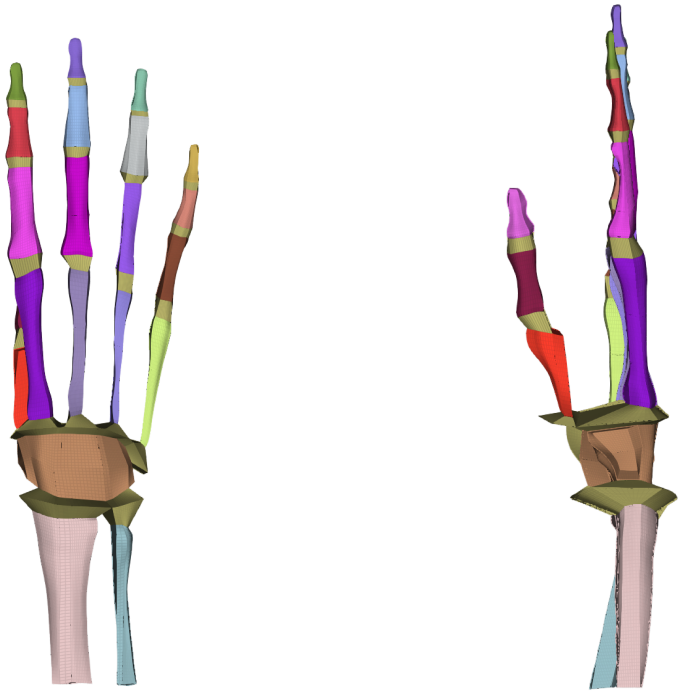

(a) Dorsal view **(b)** Side view

Figure A.3: Meshed skeleton for third thumb position model

DEPARTMENT OF MECHANICS AND MARITIME SCIENCES
CHALMERS UNIVERSITY OF TECHNOLOGY
Gothenburg, Sweden
www.chalmers.se

CHALMERS
UNIVERSITY OF TECHNOLOGY